IOP Publishing and International Atomic Energy Agency Nuclear Fusion
Nucl. Fusion **47** (2007) S608–S621 doi:10.1088/0029-5515/47/10/S10

Overview of the FTU results

V. Pericoli-Ridolfini, A. Alekseyev[1], B. Angelini, S.V. Annibaldi, M.L. Apicella, G. Apruzzese, E. Barbato, J. Berrino[2], A. Bertocchi, W. Bin[2], F. Bombarda, G. Bracco[2], A. Bruschi[2], P. Buratti, G. Calabrò, A. Cardinali, L. Carraro[3], C. Castaldo, C. Centioli, R. Cesario, S. Cirant, V. Cocilovo, F. Crisanti, G. D'Antona[4], R. De Angelis, M. De Benedetti, F. De Marco, B. Esposito, D. Frigione, L. Gabellieri, F. Gandini[2], E. Giovannozzi, G. Granucci[2], F. Gravanti, G. Grossetti[2], G. Grosso[2], F. Iannone, H. Kroegler, V. Lazarev[1], E. Lazzaro[2], M. Leigheb, I.E. Lyublinski[5], L. Lubyako[6], G. Maddaluno, M. Marinucci, D. Marocco, J.R. Martin-Solis[7], G. Mazzitelli, C. Mazzotta, V. Mellera[2], F. Mirizzi, G. Monari, A. Moro[2], V. Muzzini[2], S. Nowak[2], F.P. Orsitto, L. Panaccione, M. Panella, L. Pieroni, S. Podda, M.E. Puiatti[3], G. Ravera, G. Regnoli, F. Romanelli, M. Romanelli, A. Shalashov[6], A. Simonetto[2], P. Smeulders, C. Sozzi[2], E. Sternini, U. Tartari[2], B. Tilia, A.A. Tuccillo, O. Tudisco, M. Valisa[3], A. Vertkov, V. Vitale, G. Vlad, R. Zagórski[8], F. Zonca

Associazione Euratom-ENEA sulla Fusione, C.R. Frascati, 00044, Frascati, Roma, Italy
[1] Troitsk Institute for Innovation and Fusion Research Troitsk, Moscow Region, 142190, Russian Federation
[2] Associazione EURATOM-ENEA, IFP-CNR, Via R. Cozzi, 53 - 20125 Milano, Italy
[3] Consozio RFX, Corso Stati Uniti 4, I-35100, Padova, Italy
[4] Politecnico di Milano, Piazza Leonardo Da Vinci 32, 20133 Milano, Italy
[5] Federal State Unitary Enterprise "Red Star", 1A, Electrolitnyi Proezd, Moscow, 115230, Russian Federation
[6] Institute of Applied Physics, Russian Academy of Science, Nizhny Novgorod, Russia
[7] Universal Carlos III de la Universidad 30, 28911 Madrid, Spain
[8] Institute of Plasma Physics and Laser Microfusion, EURATOM Association, 01-497, Warsaw, Poland

E-mail: pericoli@frascati.enea.it

Received 30 January 2007, accepted for publication 11 May 2007
Published 18 September 2007
Online at stacks.iop.org/NF/47/S608

Abstract
Steady internal transport barriers (ITBs) are obtained in FTU at ITER-relevant magnetic field and density ($n_{e0} \geqslant 1.3 \times 10^{20}\,\mathrm{m}^{-3}$) in almost full non-inductive discharges, sustained by lower hybrid (LH) and electron cyclotron (EC) RF waves sources. Similarly to ITER, only electrons are directly heated which in turn heat ions via collisions and no momentum is injected. Collisions do not affect the mechanisms of turbulence suppression and energy transport. At the highest densities the ion thermal conductivity remains $\leqslant$ the ohmic level, while the energy confinement time exceeds the ITER 97-L scaling by about 1.6 times. The ITB radius can be varied in the range $0.2 \leqslant r/a \leqslant 0.65$ modifying the radial profile of the LH driven current, acting mainly on the safety factor q. A liquid lithium limiter (LLL) of innovative design, composed of a mesh of porous capillaries, has been tested successfully for the first time on a medium size tokamak. The LLL surface showed no damage up to the maximum thermal load of $5\,\mathrm{MW\,m}^{-2}$. With LLL cleaner plasmas are obtained and the particle recycling strongly drops; new interesting regimes of particle transport arise at high density, with highly peaked profiles. Significant progress in disruption mitigation by means of EC power has shown that they can be avoided when absorption occurs directly on the MHD islands driving the disruption. Feedback control/suppression of MHD tearing modes (TM, $m = 2$) with EC waves has been achieved relying on a real-time detection of the TM and of its radial location. Testing the collective Thomson scattering in ITER-relevant configuration has stressed that avoiding backscattered radiation to the source is very crucial. The theory of the evolution of fishbone-like instabilities driven by LH generated supra-thermal electrons in FTU is outlined, and its relation to the trapped α particles dynamics is stressed.

PACS numbers: 52.55.Fa, 52.50.Sw

(Some figures in this article are in colour only in the electronic version)

1. Introduction

FTU is a compact high magnetic field tokamak (major radius $R = 0.93$ m, minor radius $a = 0.3$ m, toroidal magnetic field $B_T \leqslant 8$ T, plasma current $I_p \leqslant 1.6$ MA) aimed at developing advanced scenarios at magnetic field and densities relevant to ITER operation, as well as at studying its supporting physics [1]. The FTU auxiliary heating systems, lower hybrid (LH, frequency $f_{LH} = 8$ GHz, power $P_{LH} \leqslant 2$ MW) and electron cyclotron (EC, $f_{EC} = 140$ GHz, $P_{EC} \leqslant 1.6$ MW) waves, heat electrons (e^-) and inject no momentum. Ions (i^+) can therefore be heated only via e^-–i^+ collisions. This scenario is almost unique so far in the tokamak world and allows FTU to contribute significantly to the understanding of the physics of transport in conditions of relevance for ITER. Here the main heating source will be the α-particles that interact predominantly with electrons, while the toroidal momentum, provided by neutral beam injection (NBI), is remarkably lower than in most present-day tokamaks with NBI as an additional heating source. This casts some concern on extrapolating the energy confinement of the advanced scenarios with internal transport barriers (ITBs) to ITER. Indeed the ITB dynamics is strongly affected by the high shear of the induced plasma rotation that reduces the radial correlation length of the turbulence and hence slows down the radial thermal transport. Since the advanced scenarios are very promising for a steady operation of ITER and future reactors, where the rotational shear will be negligible, the study of ITBs that are built and maintained with dominant electron heating are of particular importance.

Another crucial aspect for tokamak reactors concerns the best choice of plasma facing components (PFCs). Even though such components have already been selected for ITER, the issue remains relevant for future devices. FTU decided to advance the knowledge of the materials that are PFC candidates, by testing the properties of liquid metals such as lithium. Investigations followed two main guidelines: (i) Li as a coating film for the walls and (ii) Li as a limiter material in its liquid state. Li is appealing as a first wall material because of its low atomic number, $Z_{Li} = 3$, while a liquid divertor would definitely solve the target erosion and the cracking problems, since it can be continuously fed from the exterior. A low melting temperature (= 180.5 °C for Li) would further facilitate managing the divertor system.

Other experiments, as well as theoretical and modelling activities, have been carried out in support of ITER. On the experimental side we focused primarily on (i) the avoidance/mitigation of disruptions and the prevention/suppression of the internal magnetohydrodynamic (MHD) modes, both through the use of the EC heating (ECH) and (ii) the practicability of the collective Thomson scattering (CTS) diagnostics in the microwave frequency range ($f = 140$ GHz). The study on disruptions considered mainly the current and magnetic quench, that on internal MHD pointed to recognizing reliably and promptly the birth and the location of the mode in order to act on it in real time, that on CTS to testing the feasibility of the measurement itself. The theoretical efforts have been spent in understanding and reproducing the growth and evolution of the electron-fishbones instability observed in high-power almost full LHCD (LH current drive) FTU discharges and caused by the supra-thermal electrons. The importance of these modes for ITER resides in the fact that very similar instabilities can be driven by energetic fusion α-particles, because their dynamics depends primarily on the particle energy and not on mass and because of similar small dimensionless orbits.

This paper describes the main new results of the FTU team obtained since the last Fusion Energy Conference (FEC) [2]. Inevitably, most of them have already been dealt with in several already published papers [3–6] or are in preparation [7], from which more detailed information can be retrieved. The present review is organized as follows. Section 2 describes the progress in the advanced tokamak scenarios and section 3 the results obtained with LLL. Section 4 deals with disruption mitigation while section 5 deals with the active control of the MHD instabilities by means of the EC power. In section 6 the CTS diagnostic test is summarized. In section 7 other activities in support of the tokamak physics, namely, the LHCD physics, are briefly reviewed. Theoretical understanding of the dynamics of the electron-fishbones is presented in section 8. Conclusions are drawn and a brief summary on the work carried out in the years 2005–2006 is given in section 9 together with the near-term perspectives.

2. Advanced tokamak scenarios

The FTU program on e^-ITBs addresses several aspects of the physics related to their onset, control and sustainment. One of the more ITER-relevant issues is to ascertain whether the high density and the electron–ion collisional coupling influence the ITB dynamics and whether an ion transport barrier could develop in the presence of e^- heating only. This latter point would greatly clarify the role of the many candidate mechanisms for the ion turbulence stabilization. Both these issues well match the FTU potentialities that are complementary to those of other devices engaged in similar research areas. Regimes of dominant electron heating in JET still have ions heated by NBI, overwhelming the collisional heating, and have a non-negligible NBI-driven current fraction [8]. TCV is equipped with pure electron heating systems but operates at densities much lower than FTU [9]. Conversely, Alcator C-mod operates at densities even higher than FTU but had a limited CD (current drive) capability [10] until the recent addition of a 1 MW LH system [11]. Asdex-U can also approach high density regimes [12] but it has only NBI as additional heating. On the other hand, FTU cannot deal with questions related to the role of fast ions, since there is no way to produce them, or to the high ß, due to its high magnetic field (ß $= 2\mu_0\langle p\rangle/\langle B^2\rangle$, μ_0 = vacuum magnetic permeability, $\langle p\rangle$ average plasma pressure). Neither can it investigate the divertor physics, being a limiter device. Further details on FTU are in [1].

Stationary ITB regimes, candidates as a steady scenario for ITER, have been established in almost full CD conditions at the ITER working density and magnetic field. A previous work [3] reported on the high density steady ITBs, with the central density $n_{e0} \geqslant 1.3 \times 10^{20}$ m^{-3} ($n_{e0}/n_{GW} \geqslant 0.9$, n_{GW} = Greenwald density limit [13]) and central electron temperature $T_{e0} \geqslant 5$ keV. The energy confinement time is enhanced by 1.6 times with respect to the ITER97-L scaling, which is applicable to FTU, and ion collisional heating does

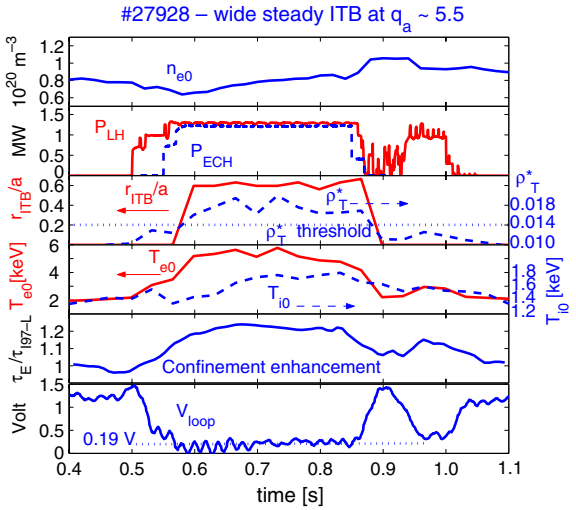

Figure 1. Time evolution of the most significant parameters for #27928, the widest steady ITB; co-ECCD configuration slightly off-axis (≈6 cm). $I_p = 0.51$ MA, $B_T = 5.3$ T, $q_a \approx 5.4$.

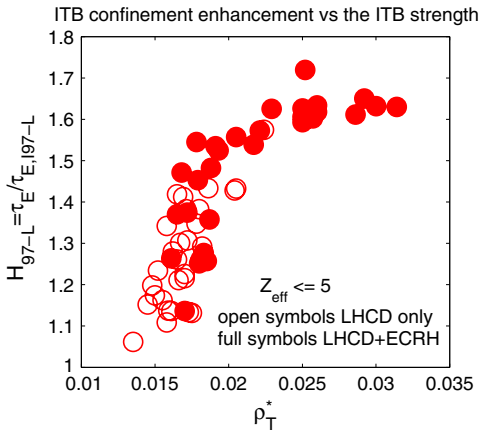

Figure 2. Global energy confinement of the ITBs, shown as the enhancement over the ITER97-L scaling versus the barrier strength.

not affect the barrier dynamics. The barrier was however not wide. Since then, methods to control the barrier radial width by LHCD have been successfully developed, even though limited so far to regimes with $n_{e0} < 0.9 \times 10^{20}\,\mathrm{m}^{-3}$. Steady ITB radii up to $r/a \leqslant 0.67$ have been obtained by peripheral LH absorption, favoured primarily by operation at low safety factor q [14].

The time traces of the most relevant parameters of a steady wide barrier are presented in figure 1. The q value at $r = a$ is $q_a = 5.4$, for $B_T = 5.3$ T, $I_p = 0.5$ MA and $n_{e0} \sim 0.8 \times 10^{20}\,\mathrm{m}^{-3}$ (upper frame). Density cannot be further raised at this current with the given available power, since the driven current fraction, which is a key parameter for the appropriate current density profile $j(r)$, and hence $q(r)$, is $I_{CD}/I_p \propto P_{LH}/(n_e \times I_p)$. The product $n_e \times I_p$ is here a bit smaller than at the highest density ITB (0.36 MA $n_{e0} \sim 1.3 \times 10^{20}\,\mathrm{m}^{-3}$) because of the geometric effect: the driven current is spread over a wider surface (r_{ITB} is larger) and its effect on the shape is decreased. In this kind of discharges the contribution of off-axis ECCD ($r_{ECCD} \sim 0.2 \times a$, r_{ECCD} = minor radius of the ECCD deposition) is essential to build the barrier [15]. Conversely, in narrower, higher density ITBs it is often very useful to have a counter ECCD at the centre in order to remove more efficiently the ohmic current there [16].

In the third frame the radial extension, r_{ITB}/a, and the strength of the barrier are plotted. The strength is given as $\rho^*_{T,Mx}$, the maximum of the normalized T_e gradient $\rho^*_T = \rho_{L,s}/L_T$ ($\rho_{L,s}$ = Larmor radius of the ions at the sound velocity and $L_T = T_e/(\mathrm{d}T_e/\mathrm{d}r)$). They are both quite steady all along the heating pulse. The ITB extends beyond $r_{ITB}/a > 0.6$, while $\rho^*_{T,Mx}$ is ~0.019, well above the ITB threshold, $\rho^*_{T,th} = 0.014$ [17] but below the best values achieved in FTU, larger than 0.03. As previously shown [3, 16], r_{ITB} is primarily determined by the shape of $q(r)$ and hence by the LHCD radial profile in our almost full CD discharges, and it is independent of ρ^*_T. The central q value is $1 < q_0 < 2$, then a low or weakly inverted magnetic shear region with $q_{min} \approx 1.2$–1.3 (shear is defined as $s = r/q \times \mathrm{d}q/\mathrm{d}r$) follows, at whose end the ITB foot is located, generally close to where $q \approx 1.5$ [3]. In these wide ITBs the $q(r)$ profile resembles that of hybrid regimes [8]. The link in FTU of the ITB foot with a low-order rational q value surface and the effect of the low magnetic shear agree well with the JET observation [18–20], despite the quite different ITB genesis. In FTU the LHCD pulse starts almost always during the current flat-top, while at JET at the very beginning of the discharge, as also in JT60-U [21]. Early LHCD, when $q(r)$ is far from the relaxed shape, the shear is still deeply reversed and $q_{min} > 2$, is not allowed in FTU by various constraints [16].

The time evolution of the central electron and ion temperatures is plotted in the fourth frame. The magnitude of $\Delta T_{i0} \geqslant 400$ eV is at the top of the FTU values and has allowed us to carry out an analysis of the ion transport, as described below. The much smaller value of ΔT_{i0} with respect to ΔT_{e0} is because the thermal e^-–i^+ equilibration time, $\tau_{th,ei}$, is much longer than τ_E, the global energy confinement time. The figure shows that saturation in T_{i0} is attained about 0.1 s after the electrons, consistently with the estimated $\tau_{th,ei} \sim 0.2$ s, while $\tau_E \sim 0.03$ s.

In the fifth frame is plotted $H_{97-L} = \tau_E/\tau_{E97}$, the confinement improvement over the ITER97-L scaling [22], which is appropriate for FTU. This ratio is ~1.2 only because the barrier is not strong. Values ⩾1.6 have been obtained for the rather high density, but narrower, ITBs [3].

Finally the bottom frame shows the residual loop voltage, corresponding to an OH current less than 20%. The bootstrap current fraction I_{bs}/I_p is <10%. $I_{bs}/I_p > 30\%$ is obtained in the strongest ITBs [3, 16].

The dependence of the confinement on $\rho^*_{T,Mx}$ is presented in figure 2, where full and open symbols discriminate between LHCD alone and LHCD+ECH. The improvement is fast for $\rho^*_{T,Mx}$ just beyond the threshold of 0.014, then it slows down remarkably and probably saturates at $H_{97-L} \approx 1.7$. This is clearly consistent with stabilization of turbulence occurring just at a critical gradient. Evidence of this stabilization around the ITB radius is given in [3, 23].

Noticeably, figure 2 shows that $\rho^*_{T,Mx}$ is a very good parameter to describe the quality of the confinement in FTU. The radial size of the barrier, which varies in a quite wide range $0.2 \leqslant r_{ITB}/a \leqslant 0.65$, appears instead almost non-influential. We interpret this as a balance between two conflicting facts

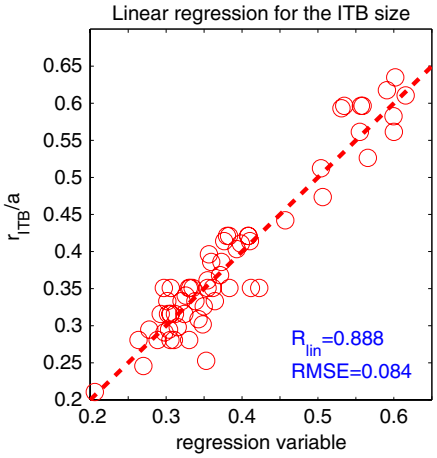

Figure 3. Linear regression analysis for the ITB radius normalized to the plasma radius. $R_{\rm lin}$ stands for linear correlation factor, RMSE stands for root mean square of the error and the regression variable is $10.5 \cdot q_a^{-1.23}\ (I_{\rm CD}/I_{\rm p}^{0.331}\ Z_{\rm eff}^{0.165}\ T_{\rm e0}^{0.261} \bar{n}_{\rm e}^{-0.24}\ N_{\|0}^{-0.15}\ B_{\rm T}^{-0.806}$.

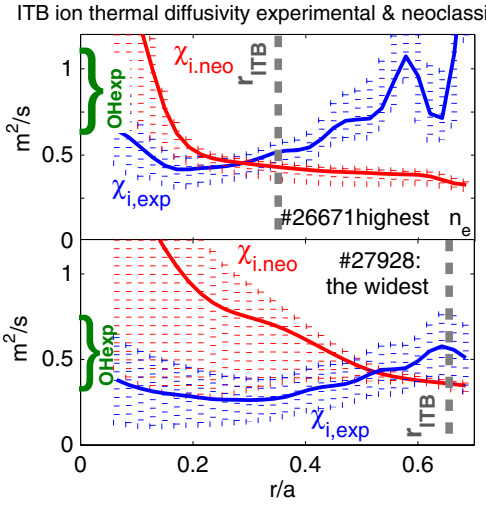

Figure 4. Ion thermal conductivity, the highest density (top) and the widest (bottom) steady ITB. The full lines give the values averaged over the whole ITB phase. The dashed vertical bars are the associated errors. For the neoclassical values they come mostly from the uncertainties in the $q(r)$ profile. On the ordinate axis the symbol '}' identifies the range of the experimental $\chi_{\rm i}$ in the ohmic phase.

occurring when $r_{\rm ITB}$ varies. If the ITB widens, on one hand the confinement improves because of the increased volume, but on the other hand it decreases because $\rho_{\rm T}^*$ is reduced. Indeed, more particles inside the ITB have to share the available power: the average increment of $T_{\rm e}$ must drop together with $\nabla T_{\rm e}$ and hence ρ_T^*. Consistently the discharges with the highest improvement in the confinement are those with strong central ECH: a direct experimental evidence of that is given in [16]

The ITB radius still remains a crucial parameter since it always delimits the region suitable for fusion processes and hence their total number. The radius in e^-ITBs is very strictly linked to $q(r)$, as stressed above, and then to the deposition radial profile of the external CD source, if the OH transformer and other mechanisms possibly affecting $j(r)$ can be neglected. This occurs for FTU, as discussed in [3], where the contribution of LHCD, ECCD (co- and counter) and OH (especially counter) is discussed.

With the view of realizing an active control of $r_{\rm ITB}$, its dependence on the principal parameters was searched for. The results of the regression analysis over the whole FTU database are given in figure 3 for the $r_{\rm ITB}/a$ ratio. In addition to the driven current fraction, most important are those quantities that were recognized in [24] to affect the propagation and the radial absorption of the LH waves. Reference [3] gives direct experimental evidence that primarily a q_a decrease but also a $T_{\rm e0}$ increase broaden and shift outwards the LH absorption. Conversely, the strong influence of $B_{\rm T}$ appears to be linked only to the definition of $\rho^*{}_{\rm T} \propto 1/B_{\rm T}$. Other indicators of the barrier strength such as $R/L_{\rm T}$ do not show this trend. Reference [24], instead, discusses how the other quantities of the regression variable can alter the launched $N_\|$ spectrum through scattering in the edge plasma and modifications suffered along the ray trajectory.

An important contribution to understanding the properties of ITBs driven by pure e^- heating and CD methods is the analysis of the ion transport, performed with the transport code JETTO on the basis of the ion temperature profiles, $T_{\rm i}(r)$, deduced from the neutron camera [25]. The results are shown in figure 4 where the ion thermal conductivity, $\chi_{\rm i}$, during the ITB is plotted as a function of the radius for the most representative steady discharges, that obtained at the highest density (top) and that at the largest radius, the same as in figure 1 (bottom). Comparison is made between the experimental and the neoclassical values averaged over the whole duration of the ITB phase. The dashed vertical bars give the associated estimated errors.

The errors on the neoclassical values come mostly from the uncertainties on the $q(r)$ profile ($\chi_{\rm i,neo}$ is $\propto q^2$), as calculated by JETTO. In the core this results slightly higher than that suggested by the MHD activity map reconstructed from soft x-ray tomography (SXT) and consequently leads to an overestimation of $\chi_{\rm i,neo}$. Nevertheless, for two very different ITB discharges $\chi_{\rm i}$ appears to be significantly reduced at $r \leqslant r_{\rm ITB}$, at the neoclassical level at least. Furthermore, $\chi_{\rm i}$ stays below even the value that it has in the ohmic phase, where the ion temperatures are lower.

Although limited so far at low $T_{\rm i0}$ values, this result is relevant for the physics of the turbulence stabilization of the ion and the electron channels. It suggests that the same mechanisms responsible for the reduced electron transport, i.e. a proper low shear q profile, affect favourably the ion transport also, without the support of induced plasma rotation. Turbulence in such regimes indeed shows a clear drop in the overall fluctuation level close to the barrier foot and a decorrelation of the modes with $k_\theta \rho_{\rm i} \approx 0.3$ [3,23], which is in the right range for affecting both e^- and i^+ transport channels.

Extension of ITBs to higher currents and magnetic field, where the plasma performances improve, is being considered at present. The ECH power could be fully exploited even with no cold resonance in the plasma because the LH created fast electrons can efficiently absorb the EC waves, due to relativistic effects, and significantly improve the CD efficiency [5]. Predictions made by using the recent LHstar code for the LH deposition give $T_{\rm e0} \sim 8\,{\rm keV}$ for $B_{\rm T} = 8\,{\rm T}$ and $I_{\rm p} = 0.7\,{\rm MA}$ and line averaged density $\bar{n}_{\rm e} = 0.7 \times 10^{20}\,{\rm m}^{-3}$

[26]. LHstar was developed to account for the non-linear interaction of the LH waves with the edge plasma [20, 27]. The consistency of its results with experiment both for JET and FTU is discussed in [28, 26].

3. The liquid lithium limiter (LLL)

The interest in liquid lithium as a first wall material for magnetic fusion devices is incessantly growing in the world tokamak community. In the USA, extensive experimental (CDX-U) and modelling work is being carried in the framework of the US Advanced Limiter-Divertor Plasma-Facing Systems (ALPS) [29]. Indeed, divertor targets made with liquid Li could have an unlimited lifetime, due to the possibility of continuously supplying from outside a low temperature liquid (the Li melting point is 180.5 °C). This would strongly reduce the problem of erosion by thermal overloads, either transient or steady.

Li could also be an appealing alternative for the main chamber walls of a reactor than the currently envisaged Be, because of its lower atomic number ($Z_{Li} = 3$, $Z_{Be} = 4$) and much larger capability of pumping hydrogen. The upper limit at present imposed on ITER to the average plasma atomic number, $Z_{eff} = 1.5$, would be easier to meet, whereas the reduced particle recycling at walls would allow a tighter control of the plasma density. The persistence of the Li film on the walls would be assured by the almost endless source at the divertor target.

In order to advance the knowledge of Li as a suitable PFC, ENEA and two Russian institutes, TRINITI and RED STAR, started a joint programme some years ago aimed at testing a LLL of new design [30] for the first time in a high field, medium sized, carbon-free tokamak (FTU). The design novelty rests on the capillary porous system (CPS) configuration [31]. A mesh of capillary channels is fed with liquid Li by an underlying reservoir and the associated surface tension withstands the electromagnetic tearing-off J×B forces.

Here we summarize the main successful tests so far completed using the LLL as an efficient tool for wall lithization (coating the vessel first wall with a Li film) and as a suitable material facing the plasma. Then we describe the principal physical effects observed on the plasma behaviour, edge and core, distinguishing between those linked to the lithization and those more strictly caused by the actual presence of the LLL in the scrape-off layer (SOL) plasma.

This first experimental campaign has been limited to ohmic plasmas, whose main parameters range within $0.5 \leqslant I_p \leqslant 0.9$ MA, $0.15 \leqslant \bar{n}_e \leqslant 2.7 \times 10^{20}$ m^{-3}, $B_T = 6$ T. More details are in [4, 32].

3.1. Technical achievements with LLL

Lithization of the FTU walls is carried out by positioning the LLL 1–1.5 cm inside the vessel bottom during plasma discharges, with the toroidal limiter, made with the Mo-based alloy TZM, still acting as the main limiter. Thermal load, which can lift the LLL surface temperature from ∼200 °C to ∼450 °C according to infrared emission measurements [33], and particle sputtering pull gaseous Li out of the CPS edge. SOL transport mechanisms then spread Li over the whole first wall surface, vessel + toroidal limiter. A quite good and complete Li coating requires about 10^{21} atoms to be extracted from the LLL surface, corresponding to 10 monolayers deposited on the walls, and it is achieved after two or three plasma discharges. Plasma operations with lithized walls are characterized by definite predominance in the UV emission spectrum of the lithium line (the highest from Li-III is at 13.5 nm) while the O, Mo and Fe lines are strongly reduced by a factor around, respectively, 3.5, 1.8, 2.0.

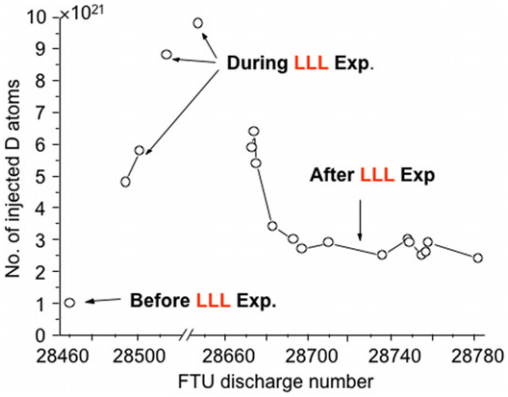

Figure 5. Total amount of injected gas into discharges at $I_p = 0.5$ MA, $B_T = 6$ T, $\bar{n}_e \sim 0.8 \times 10^{20}$ m^{-3}, versus the shot number. Clearly, after the pumping action is decayed, much less gas is required to sustain the discharge.

The LLL has been exposed to thermal loads in excess of 5 MW m^{-2} without any damage to the lithium surface or phenomena such as 'lithium bloom'. The maximum increase in temperature on the Li surface does not exceed 250 °C also for the strongest interaction with the plasma, suggesting the onset of some sort of self-protection mechanism [32]. However, transient increments up to $\Delta T_{LLL} \sim 400$ °C have been sometimes recorded which are probably due to localized hot spots whose origin is still being investigated.

3.2. Effects of the lithized walls

With 'lithized' walls the plasma appears remarkably cleaner: loop voltage, radiated power and Z_{eff} are lower than that for either purely metallic or boronized walls [34–36]. Lithized walls also exert a strong pumping action on the D_2 particles and highly reduce the recycling, as can be deduced from figure 5 where the total amount of gas puffed into the vessel is plotted versus the shot number. Plasma parameters with $I_p = 0.5$ MA, $B_T = 6$ T, $\bar{n}_e \sim 0.8 \times 10^{20}$ m^{-3} are considered. As the Li film is removed from the walls much less gas is required to sustain the discharge. This Li property allows a tight control of the density in the whole spanned range $\bar{n}_e = 0.15$–2.7×10^{20} m^{-3}. The lower density value was never attained in FTU before, while the upper value is a factor of 1.4 above the Greenwald limit. This high density can be obtained without disruption while it is not achieved with other condition techniques, as shown in figure 6, where the line density and the H_α signal are compared for two discharges, one with lithized and the other with boronized walls. For both $B_T = 6$ T, $I_p = 0.5$ MA, $n_{GW} = 1.93 \times 10^{20}$ m^{-3} and $q_a = 6.1$. As expected if the density limit is mainly due to the edge physics, the MARFE evolution is also affected. In both discharges, the MARFE

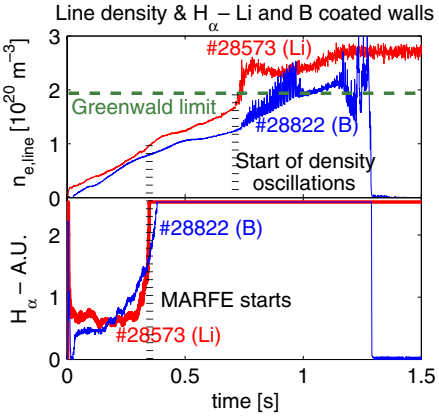

Figure 6. Time evolution of the line averaged density (top) and H_α light intensity (bottom) for two high density discharges with walls lithized or boronized. $B_T = 6$ T, $I_p = 0.5$ MA, $q_a = 6$. Two vertical dashed lines indicate when the MARFE appears on the H_α signals, at 0.3 s, and on the CO_2 interferometer, at 0.75 s.

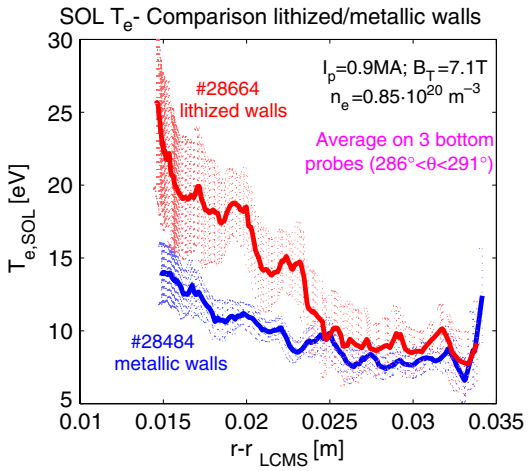

Figure 7. $T_e(r)$ in the SOL for metallic and lithized walls. Errors are shown as shadowed bands.

appears on the H_α channel at about 0.3 s (corresponding to the fast rise of the signal) and later on at about 0.75 s, on the central chord of the CO_2 interferometer as density oscillations. The two times are indicated with dashed vertical lines in the figure. The corresponding density is however higher for the lithized than for the boronized discharge: fast oscillations start at $\bar{n}_e \sim 1.6 \times 10^{20}$ m^{-3} against 1.2×10^{20} m^{-3}. More details on the effect of lithization on the density limit and the density radial profile are given in [36].

The most interesting change in the SOL parameters is the electron temperature increase with respect to metallic walls conditions, as illustrated in figure 7 for $I_p = 0.9$ MA, $B_T = 7.1$ T, $\bar{n}_e \sim 0.85 \times 10^{20}$ m^{-3}. Other cases are reported elsewhere [4]. The SOL density instead is higher for the lithized walls in this case, because of the larger amount of gas required to sustain the discharge in order to balance the strong pumping action of lithium, see figure 5. Measurements are obtained with a reciprocating Langmuir probe in the vessel bottom and are averaged over a poloidal angle $\Delta\theta \sim 5°$. At the last closed magnetic surface (LCMS) T_e increases by more than 50% with Li ($\Delta T_{e,LCMS} \sim 10$ eV), despite the amount of power

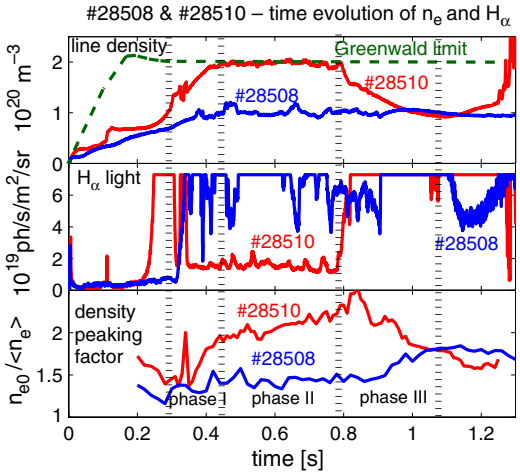

Figure 8. Line density (top), H_α light intensity (middle) and density peaking factor (bottom) are compared for two identically pre-programmed high density discharges. $I_p = 0.5$ MA, $B_T = 6$ T. #28510: LLL inserted ~1.4 cm into the main chamber; #28508: LLL left outside. The limits of the three different phases of the discharge are marked with dashed vertical lines.

entering the SOL being nearly unchanged, $P_{SOL} \sim 0.6$ MW for both discharges. This is a consequence of the much reduced radiating capability of Li inside the SOL with respect to Mo, which is such an efficient energy sink to clamp the temperature in the range 15–20 eV even upon strong additional power. Within the frame of the 2D edge physics code TECXY [37], the magnitude of $\Delta T_{e,LCMS}$ can be accounted for only if the H recycling is negligible, consistently with the strong pumping effect of the Li coating, as pointed out in [4, 38].

3.3. Effects of the LLL inside the vacuum vessel

The presence of an intense localized source of Li atoms and ions inside the vessel can deeply modify the properties of both the SOL and the core plasma. Direct evidence of the important changes occurring in the SOL is given by the pictures of a CCD camera looking at a plasma discharge, presented in [4]. A bright toroidal annular region builds up in a restricted poloidal region in between the LLL and the toroidal limiter. Just there the TECXY code foresees the development of a region across the LCMS of increased density, lower temperature and enhanced radiation loss. This is detailed in [4] where the measured SOL temperature and the density with the code predictions are also compared. Measurements are taken from two arrays of reciprocating Langmuir probes, located at two different poloidal angles, and from probes mounted on the LLL support frame, very close to the leading edge. The density increase and the temperature drop revealed on the LLL probes are consistent with both the TECXY calculations and the CCD pictures.

Under these circumstances a very interesting effect has been found in high density discharges, when $\bar{n}_e > 0.5 \times n_{GW}$, where the large recycling drop deeply affects the whole SOL dynamics and the core plasma properties, as a consequence. An enlightening example is given by comparing the time evolution of two very close discharges: #28510, with the LLL inserted 1.4 cm inside the vacuum vessel, and #28508 with LLL outside. In figure 8, the line densities are plotted in frame

(a) together with the Greenwald limit. Frame (b) shows the H_α emission light seen by one of the horizontal array detectors (all the others show a very similar behaviour); frame (c) gives the density peaking factor $f_{pk} = n_{e0}/\langle n_e \rangle$, ratio of the central to the volume averaged density value.

With LLL (#28510) a new regime is built at $t \sim 0.29$ s that lasts about 0.5 s with the following features. In phase I, the building-up phase from nearly 0.29 to 0.42 s, $\bar{n}_e$ rises up to $2 \times 10^{20}\,m^{-3}$ ($\sim n_{GW}$), twice the pre-programmed value, which is just maintained in #28508. The peaking factor grows from $f_{pk} \sim 1.5$ in #28508 up to $f_{pk} > 2$ in #28510, while the H_α light drops as in L–H transitions in divertor plasmas. In phase II, the steady phase from 0.42 to 0.79 s, the H_α light stays low indicating a strongly reduced particle recycling, whereas in #28508 the detectors' signals saturate, and $\bar{n}_e$ stays high, despite no gas being fuelled into the vessel. In phase III, the decay phase from 0.79 to 1.08 s, the quantities revert to the #28508 values, the H_α light being quite fast, while $\bar{n}_e$ takes about 0.2 s as does f_{pk}, which however shows also an initial increase.

The peaking factor during phase II is rather high for a $\bar{n}_e$ value is so close to n_{GW} and contrasts with the common observation of flatter density profiles as n_e grows. All along this phase a clear steepening of $n_e(r)$ occurs close to the edge ($r/a \sim 0.7$) [4] resembling the peculiar feature of a barrier. The barrier nature of this regime can be recognized by looking at the time evolution of the density profiles during phases I and III, which are presented respectively in figure 9(a) and (b). Non-inverted profiles, as measured by a radially scanning CO_2 interferometer [39] at different times along several vertical chords, are considered here, in order to avoid any mathematical artefact due to the inversion process.

Figure 9(a) clearly shows that a density pedestal is first established at the very periphery, and then the outer layers are depleted in favour of the inner ones. This net inward flux is not balanced by an equal flux of particle across the LCMS, because of the low number of neutrals in the edge plasma. The peaked profiles maintain until the pedestal is destroyed, between 0.77 and 0.79 s (look at the dashed trace in figure 9(b)). First, the outermost layers are depleted by a net outward flux, this time. Consistently, in the early phase III the density peaking rises further and the H_α light hugely increases, figure 8(c). Then follows the loss of particle also from the core.

The formation of a particle transport barrier is testified by the quick change in the slope of the traces at $r/a \sim 0.7$, evidenced by a grey rectangle in the figures, that lasts all along phase II. The importance of this radius, which could be assumed as the barrier footprint, is further stressed by the observed changes in the transport coefficients. Reference [4] shows that only external to it the particle diffusion coefficient and the pinch velocity vary both in the same direction of reducing the outward flux, with respect to phase III.

Also an energy transport barrier develops, though quite weak, as shown in figure 10. In the top frame are plotted $T_e(r)$, averaged over the whole phase II, and the fit used for calculating the normalized temperature gradient $\rho_T^*(r)$ (= barrier strength). ρ_T^* (bottom frame) exceeds the threshold just as $r/a \sim 0.7$, with a maximum of $\rho^*_{T,Mx} \sim 0.016$. The plasma is not detached from the limiter since the LCMS temperature and the density are almost equal to the values in the reference

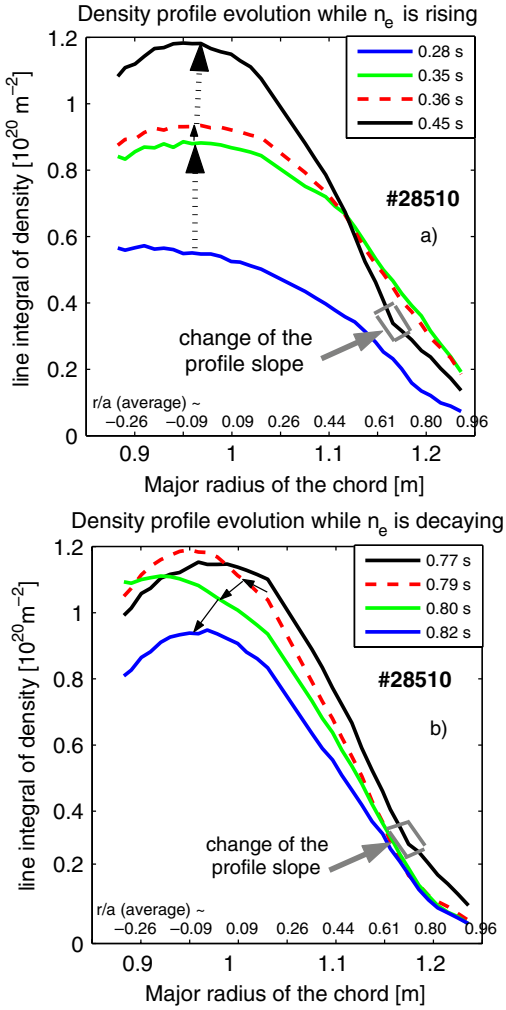

Figure 9. Time evolution of the line averaged density profile plotted versus the interferometer chord impact parameter, during the build-up (frame (a)) and the decay (frame (b)) phases of the high density regime. These profiles are shown non-inverted to get rid of any numeric artefact of the inversion technique. Are clearly visible in (a) the onset of pedestal and a re-adjustment of the outer part of the profile due to the changed transport characteristics and in (b) the almost simultaneous loss of pedestal and the depletion of the outermost plasma layers (dashed curve).

pulse #28508, respectively, ~15 eV and $\sim 1.5 \times 10^{19}\,m^{-3}$ [4]. The global energy confinement improves over the ITER97-L scaling [22] by 1.16 times, consistently with the data of figure 2. However, compared with other discharges without LLL and with the same, $\bar{n}_e$, I_p and B_T, τ_E does not emerge definitely above the variability range, yet being at its top.

Both the exact conditions to access this enhanced confinement phase and the reasons for its termination are at present under investigation. Working hypotheses are that the details of the plasma–LLL interaction may strongly affect the production of gaseous Li and influence accordingly the physics of the particle recycling and refuelling, see [4].

4. Disruption mitigation with ECH

Experiments devoted to disruption avoidance by means of ECH power (up to three gyrotrons $P_{ECH} \leqslant 1.2$ MW) have been

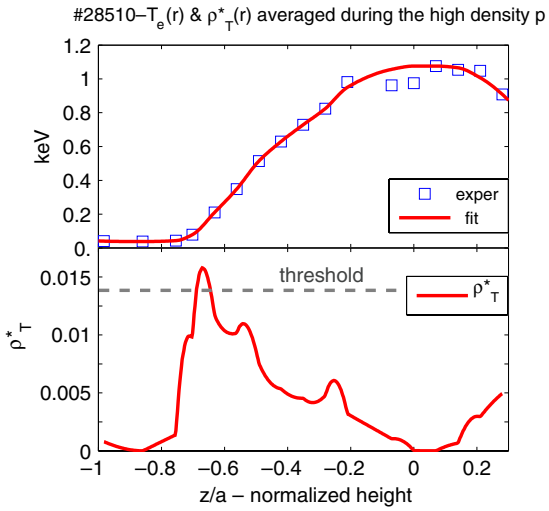

Figure 10. Upper frame: radial profiles of the electron temperature averaged over the whole high density phase (□) together with the fit used to evaluate the gradients (full line). Lower frame: radial profile of the normalized temperature gradient $\rho_T^*(r)$.

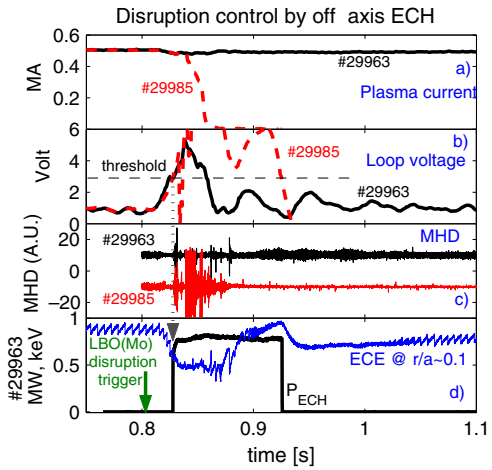

Figure 11. Time evolution of two discharges with (#29963) or without (#29985) off-axis ECH to mitigate/avoid disruption. (*a*) Plasma current; (*b*) loop voltage with the chosen threshold level for ECH injection; (*c*) MHD activity monitor; (*d*) #29963 only: ECH power and a quite central ECE channel. The recovery of the pre-disruption situation is indicated by sawteeth reappearing at ∼1.05 s in the ECE.

performed in deuterium plasmas discharges with $B_T = 5.3$ T, corresponding to on-axis EC resonance. Off-axis deposition is obtained by steering poloidally the launching ECH mirrors that can focus the power above or below the equatorial plane up to the very edge. Disruptions are driven either by injection of Mo through laser blow-off (LBO), in plasmas with $\bar{n}_e = 0.6 \times 10^{20}\,\mathrm{m}^{-3}$, $I_p = 0.5$ MA, $q_a = 5.2$, or by raising $\bar{n}_e$ above the density limit in 0.36 MA discharges ($n_{GW} \sim 1.2 \times 10^{20}\,\mathrm{m}^{-3}$) with a properly pre-programmed gas puffing. ECH power is triggered by the loop voltage V_{loop} exceeding a certain threshold, namely $V_{loop} > 3$ V. The choice of a correct and reliable disruption precursor as well as of the type of impurity and the amount to be blown off in order to get reproducible disruptions has been part of research activity [40].

Figure 11 shows the time traces of the most relevant quantities for the case of Mo-injection when the disruption

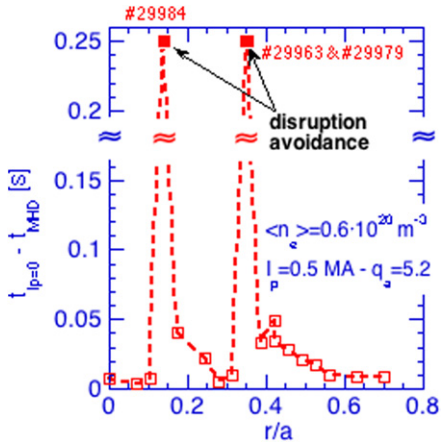

Figure 12. Scan over the deposition radius of the ECH power in a series of discharges equal to that shown in figure 11. To avoid disruption the correct localization of the ECH absorption on the growing MHD island is essential.

is completely avoided and the discharge terminates as if it had been unperturbed. This is inferred from the electron cyclotron emission (ECE) signal in frame (*d*) that 200 ms after ECH application displays again sawteeth as before LBO. In this case ECH is deposited off-axis (at $r/a = 0.35$) and it is applied during the energy quench just before the onset of strong MHD activity (figure 11).

The preliminary results of an ECH power deposition radial scan are presented in figure 12. The difference between the time of the beginning of the current quench and the time of the start of the MHD activity is plotted against the ECH deposition radius, as determined by geometrical considerations only on the orientation of the launching mirrors. Disruption is avoided only when the power is absorbed in the narrow region where MHD islands develop, according to SXT reconstruction. The very limited radial range of effectiveness for ECH power deposition clearly indicates a direct and local effect on the growth of the islands: a detailed analysis is underway and will be the subject of a future paper. A brief ECH application is enough for the purpose: from the ECE trace of figure 11 frame (*d*), a full recovery occurs within 75 ms.

A natural evolution of this line of research is the possibility of real-time fast localization and heating of the growing island, before the power necessary to avoid the disruption exceeds the available power. The time lag available for the purpose is longer than 10 ms, as inferred from figure 11 by comparing the time traces of the plasma current, loop voltage and MHD activity of the two discharges. As shown in the next section, this time is in reach of the newly developed technique on FTU, based on the cross-correlation between ECE channels and between ECE and MHD coils, capable of early recognizing the growth and location of MHD modes.

Few experiments with density limit disruptions have been carried out so far due to operational problems caused by the EC cut-off at high density [5]. Disruptions have been avoided with almost central deposition ($r/a = 0.08$, $P_{EC} = 0.8$ MW) even after the start of considerable MHD activity: stabilization of the $m/n = 3/2$ mode is the probable cause of such disruption avoidance. Off-axis ($r/a = 0.7$) ECH absorption has not been found effective, but the absorbed power was very poor

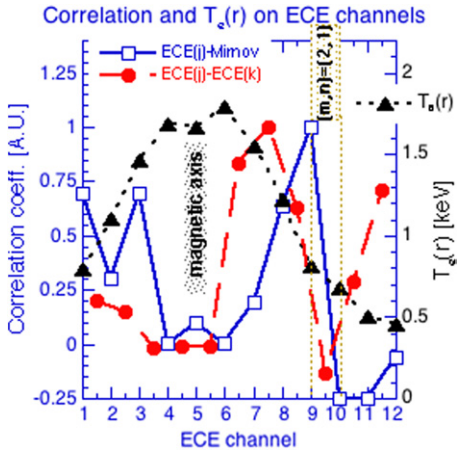

Figure 13. Correlation between nearby ECE channels (λ) and between ECE and Mirnov coil signals (●). T_e profile deduced from ECE is also plotted (▲).

(∼10%) due to low temperature. Experiments are in progress to optimize the ECH timing and to increase the database of density limit disruptions.

5. MHD mode control

The absorption of EC waves is very localized on a tokamak and hence can directly affect the helical currents sustaining the tearing mode (TM) MHD instability, leading to its suppression. The automation of the stabilizing action, needed in a fusion reactor, can be achieved by a 'smart EC Waves launcher' capable of reliable and fast reaction to MHD, by zeroing the distance between the island position r_{island} and the deposition radius r_{dep} [41].

The measure of r_{island} can be performed by a spatially resolved measurement of T_e oscillations (ECE radiometer is the best option) naturally induced by the TM rotation. The π phase jump on opposite sides of the island can be used in principle to locate r_{island}. In practice, the island is located where a minimum correlation in adjacent ECE channels is observed [42]. In order to increase the robustness of r_{island} detection against noise and sawteeth influence, a Mirnov coil provides a reference signal for a dynamic ECE filtering around TM frequency.

The r_{dep} measurement is usually accomplished by modulating the EC power and looking for the peak in synchronous T_e oscillations. In the case of multiple beam applications, each r_{dep} can be distinguished by a different modulation frequency [41].

In FTU we demonstrated the impact of ECH on MHD of coupled modes [43], stabilized TMs by properly aligned ECH [44] and finally achieved automatic stabilization [45].

The technique used to localize a MHD mode is shown in figure 13 as the correlation between adjacent ECE channels of a 12-channels polychromator and the correlation between each ECE and a Mirnov coil signal. ECE_i/ECE_j correlation shows a clear minimum at ch.9/ch.10. Correspondingly, ECE/Mirnov correlation changes sign from ch.9 to ch.10. A (2,1) mode, as confirmed by SXT, is unambiguously located between ch.9 and ch.10.

Two gyrotrons (G1 and G3) are used for these experiments. Their power is absorbed at a position corresponding to ECE ch.7 (G1) and to ch.10 (G3). In order to allow r_{dep} detection, G1 is modulated at 250 Hz and G3 at 300 Hz. The duty cycle is normally low in the 'watch mode', i.e. it is modulated at low average power only for r_{dep} detection. During stabilization, r_{dep} monitoring is continued by complementary modulation at high average power.

Figure 14 shows the results of two real-time stabilization experiments. On the left an internal disruption destabilizes the (2,1) mode at $t \approx 0.56$ s. After 20 ms of integration time, the mode is recognized and located between ECE ch.9 and ch.10 (see also figure 13). G3, absorbed in the position corresponding to ECE ch.10, is switched to high duty cycle, while the other gyrotron continues unchanged. After ≈100 ms stabilization is completed and G3 returns to low average power. In the discharge shown on the right, the mode is destabilized when the EC stabilization system is not yet enabled. However, mode recognition is active and G3 is switched to high average power as soon as the automatic control is enabled.

6. CTS diagnostic studies

Among the other ITER oriented experimental activities of special relevance has been a reliability analysis of the mm-wave CTS diagnostic in the configuration with propagation below the EC resonance, $f_{gyr} < f_{EC}$, proposed for ITER. Indeed, a recent feasibility study [46] clearly stated that the CTS diagnostic of the fast ion populations in ITER will require propagation in the X mode at $f_{gyr} = 50$–60 GHz, to be compared with $f_{EC0,ITER} = 151$ GHz ($B_{T0,ITER} = 5.4$ T). The possibility of performing such an analysis is peculiar to FTU, because of its high magnetic field.

The wave source is a gyrotron at $f_{gyr} = 140$ GHz, also used for ECH. The experiment has been run with $7 < B_T < 8$ T, corresponding to $196 \leqslant f_{EC} \leqslant 224$ GHz. As reported in a dedicated paper [6], interesting results followed the unambiguous interpretation in 2006 of strongly anomalous non-thermal spectra systematically observed. Here we limit to the summarization of the main results.

Figure 15 shows a side view of the geometry of the incident and the scattered beams. The scattering volume was normally placed on the vessel axis. The anomalous spectra, a typical example of which is shown in figure 16, were detected in both aligned and misaligned antenna conditions. Their spectral power density (up to 70 keV in figure 16) is in all cases several orders of magnitude higher than that predicted for the ion thermal feature, 0.5 keV. At its origin the spurious signal underlying these spectra is even stronger since it is collected after multiple wall reflections and therefore subject to antenna decoupling (∼50 dB).

Attempts at explaining the anomalous spectra in terms of plasma–wave processes soon failed. Tests performed on purpose with the signal picked up directly from the transmission line, hence before the wave beam enters the plasma, revealed that these spectra were produced even in the absence of plasma provided a toroidal magnetic field was applied. This led to investigate the possible effects of resonances and cut-offs in causing unexpected back-reflection of the beam power. In the CTS configuration, with $f_{gyr} < f_{EC}$,

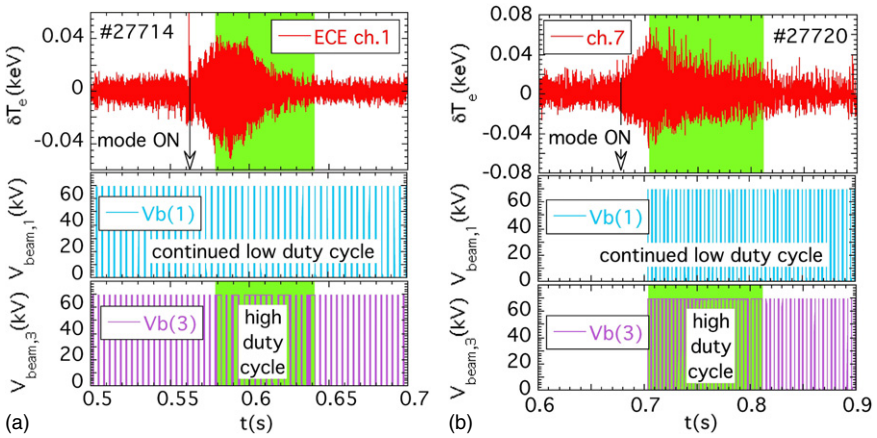

Figure 14. Stabilizing effect of ECH in two different discharges. Top to bottom: oscillation in the T_e observed in one ECE channel, the beam voltage applied to gyrotron G1 and G3. The EC power from the two gyrotrons is absorbed at two different radii.

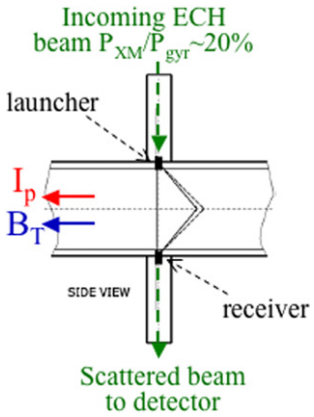

Figure 15. Side view (toroidal section) of the CTS geometry.

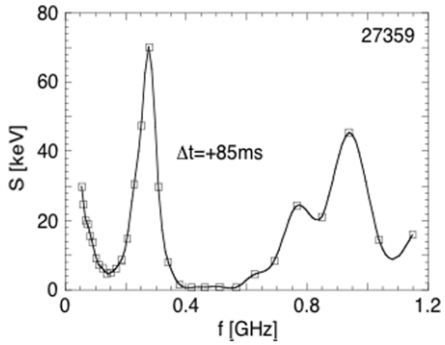

Figure 16. Typical anomalous spectrum exhibiting a relatively weak smooth low-frequency feature and strong spectral lines both at low and high frequencies. Different from the spectral lines, the smooth low-frequency feature is common to all anomalous spectra. Its spectral power density can vary up to two orders of magnitude from shot to shot. Pulse length: 380 ms; integration time: 30 ms. $B_{T0} = 7$ T, $P_{gyr} = 307$ kW $\tilde{n}_e = 0.75 \times 10^{20}$ m^{-3}, $T_{e0} = 2$ keV.

an electron cyclotron layer, an upper hybrid layer and the right-handed cut-off for the X mode (XM) are unavoidably crossed by the probe beam when propagating in the injection port. In these conditions whenever a mode mixture is injected, as was in our case, the power fraction in the X mode can be partially reflected at the cut-off layer, provided a breakdown plasma converting the three critical layers from latent to active is excited by the beam itself.

Reconstruction of the magnetic field isolines in the beam injection port showed that the EC layer was located near the port mouth. Slightly outer, but quite close to it are the other two critical layers. A strong confirmation of our interpretation was obtained at the end of the campaign, when wakes were detected on the last two antenna-mirror surfaces [6] at a location and with an inclination corresponding to the resonant isolines for $B_{T0} = 7.2$ and 8 T, the magnetic field values most frequently used.

Peculiarities of the layout may have contributed to strengthening the gyrotron perturbation in our specific case. Nevertheless the risk for this perturbation to occur in CTS experiments with $f_{gyr} < f_{ec}$ can be considered quite generally. Transmitting antennas where the critical layers remain in any case latent, independently of the propagation conditions and the power levels involved, are therefore better adopted in these experiments.

Of several alternatives considered so far the most viable seems a solution based on a remote-steering antenna (RSA) [47] with a vacuum-tight ceramic (or diamond) window at its mouth on the plasma side. A RSA of special interest for CTS in FTU was fruitfully tested in ECCD experiments on TRIAM-1M [48].

These results point out some constraints on the transmitting antenna and provide positive indications to overcome them, that can be easily extended to the mm-wave CTS diagnostics in ITER, considering the MW power level at which diagnostics will operate.

7. LHCD physics study

The work carried out on this topic in FTU dealt mainly with the analysis of the physical mechanisms affecting the LH wave propagation and absorption, since both can greatly impact on optimizing the LHCD performances in a reactor. The behaviour of CD efficiency, η_{CD}, has been investigated over the whole FTU database and the modelling of linear and non-linear interaction of the LH waves with the edge plasma was started.

The CD efficiency has also been studied in the very peculiar situation when extra power is deposited directly on the LH-generated fast electrons, ECH in our case. This happens beyond any doubt when the fundamental e^- resonance is removed from the plasma by increasing B_T (we never have higher order harmonics). In these so-called downshifted conditions, the increase in the magnetic field balances a proportionally equal relativistic e^- mass increase so that the resonance conditions are kept unchanged. Exhaustive studies have shown that, if the pre-existing fast electrons are enough to ensure an efficient ECH absorption ($\geqslant$80%), the CD efficiency calculated with the total amount of the power, LH+ECH, is unchanged with respect to LH alone. Since no direct CD can be attributed to the ECH waves, which are launched perpendicularly to B_T, an improvement takes place in the current carrying capability of the supra-thermal tail by the same amount as for LH. For more details see [5, 24].

The statistical analysis of η_{CD} dependence on the major plasma parameters, recently done in [24], has clarified the physical reasons for the spread, close to a factor of 3, in the experimental values, found in conditions of LH ray accessibility to the plasma core to be always quite good. The main causes have been identified first in the electron temperature of the target plasma, which substantially determines the form of the fast e^- tail in the parallel velocity space, and secondarily in the modifications suffered by the $N_\parallel$ (parallel index of refraction) spectrum along the ray trajectory before the power is absorbed. To the change of the $N_\parallel$ spectrum contributes non-negligibly the interaction of the LH waves with the edge plasma. The parametric dependence found in the quoted paper is consistent with linear scattering of the LH rays on the density fluctuations inside the edge turbulent layer, in agreement with a previous work on Asdex at a much lower frequency ($f_{LH} = 2.45$ GHz) [49].

In this context we started to model the turbulence in the SOL as if it were of electrostatic drift-wave nature. The most important parameters are the wave vector, which is expected to be negligible in the toroidal direction and of the order of $k_\perp \rho_i \sim 0.1$–0.3 perpendicularly, and the level of the density fluctuations, whose usual range in a tokamak is $\delta n_e/n_e \sim 0.2$–0.5 for B_T in the range 2.1–6 T [49, 50]. These two quantities are adjusted in order to reproduce the spectral shape of LH pump scattered radiation, according to the model proposed in [51]. Then the modified $N_\parallel$ spectrum exiting the scattering layer, computed again following [51], is given as input to the LH fast ray tracing code module (FRTC, [52]) of the ASTRA transport code. The poloidal extension of the LH grill, quite wide in FTU ($\Delta\theta_{LHgrill} \sim 76^\circ$), is sampled on five angles symmetric with respect to the equator. More details on this first modelling are given in [53]. The calculated radial profile of the LH absorption is then compared with that of the hard x-ray (40–220 keV) bremsstrahlung due to the LH-generated fast electrons. Here we only show in figure 17 the case of the ITB discharge #27928, considered in section 2 (see figure 1). The good agreement between experiment and model only for the modified $N_\parallel$ spectrum stresses the importance of taking into account the phenomena occurring at the edge.

Non-linear interactions are also considered in our effort to reach an agreement between measured and calculated radial profiles. A modelling (LHstar code) able to provide LH deposition profiles was produced by retaining the non-linear wave physics of the plasma edge, as well as by performing consistently the ray-tracing and the Fokker–Planck analyses [20, 27, 28]. The $N_\parallel$ spectral broadening occurring at the edge can substantially affect the radial deposition and CD, even if it affects a small fraction of the power ($\leqslant$10%). The profiles so obtained are in agreement with those inferred from the available diagnostics, FEB camera for FTU, MSE for JET. In these works it is also pointed out that the relatively high SOL electron temperature, obtained with the Li-coated vessels walls could be very helpful to let the LH waves penetrate into the bulk at high plasma density regimes, since this would greatly reduce the spectral broadening of the LH pump, resulting from the non-linear physics of the interaction LH waves-edge. It is indeed known that in such regimes the LH is deposited very peripherally, despite linear theory predicting a good penetration into the bulk.

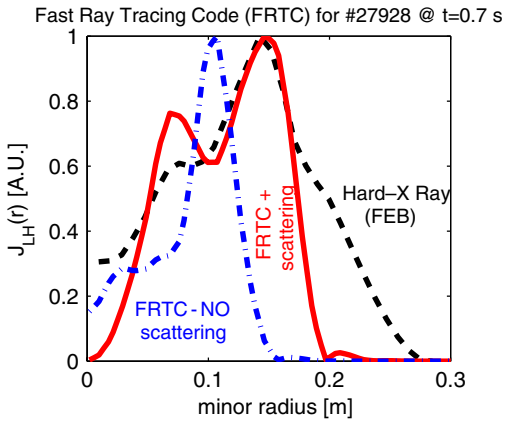

Figure 17. Comparison between the LHCD radial profiles in FTU for the case computed by FRTC accounting for the LH wave edge scattering by density fluctuations (full line), the usual one with no scattering (dashed–dotted line) and the experiment (dashed line).

8. Theoretical analyses of electron-fishbone dynamics

An example of the significant and positive feedback between theory and experimental observations is the explanation of the processes underlying the excitation of fishbone-like internal kink instabilities driven by supra-thermal electrons. A detailed theoretical analysis of these modes is given in [7], along with an interpretation of the experimental results, which have strongly motivated this study.

The peculiarity of FTU observations with respect to previous and similar ones (see, e.g. [54]), where the supra-thermal electron tail was associated with the high field side ECH, is the excitation of electron-fishbones in the presence of LH power injection only [55]. Due to the frequency gap in the low-frequency shear Alfvén continuous spectrum for modes propagating in the ion diamagnetic direction, effective electron–fishbone excitation favours conditions characterized by supra-thermal electron drift-reversal, consistently with experimental observations [54, 56]. For the same reason, the spatial gradient inversion of the supra-thermal electron tail is necessary, explaining as to why ECRH excitation is observed with high field side deposition only [54, 56].

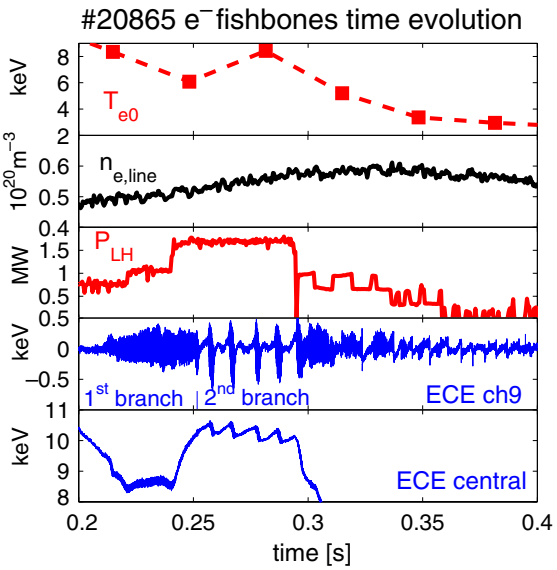

Figure 18. Time evolution (from top to bottom) of thermal e^- temperature, plasma line density, LH coupled power, fast e^- temperature fluctuations and central radiation temperature. The latter shows collapses synchronous to the fishbones activity, displayed in the frame above, which redistribute the supra-thermal population over the radius. Clearly the non-linear behaviour of the electron-fishbones reflects the level of LH power.

The case of mode excitation by LH only [55] follows the same physics with few additional twists. The fast electron populations that effectively excite the mode are the trapped and barely circulating particles (see [7] for a precise classification of particle orbits and their peculiar role). Meanwhile, LH power forms a parallel as well as a perpendicular fast electron tail (via Coulomb collisions), which is moderately slanted towards the counter-current direction, i.e. despite that the fact it guarantees the inverted spatial gradient of the supra-thermal tail, it is less selective than high field side ECRH in producing particles with drift-reversal. Thus, in the case of mode excitation by LH only, the presence of circulating supra-thermal particles is crucial for two reasons: (i) barely circulating particles effectively contribute to the mode excitation and (ii) well-circulating particles modify the current profile, eventually reversing the magnetic shear inside the minimum-q surface and broadening the fraction of trapped particles characterized by drift-reversal. Note that this effect directly modifies the kinetic contribution to the internal kink potential energy and is not associated with the MHD (fluid) potential energy change, controlled by LH power via current profile modification, as recently discussed while explaining HT-7 observations [57].

As in the case of ion-fishbones [58], two branches of the electron-fishbone exist: a discrete gap mode and a continuum resonant mode. The latter does not generally require either drift-reversal or inverted spatial gradient of the supra-thermal tail; however, it has a higher excitation threshold and, thus, it is unfavoured, particularly for the branch propagating in the electron diamagnetic direction.

The two modes, excited on FTU with different levels of LH power inputs, appear on (fast) electron temperature fluctuations with very distinctive signatures (see figure 18), characterizing the non-linear physics of e$^-$-fishbones. During the high power LH injection, an evident transition in their signature takes place from almost steady state non-linear oscillations (non-linear equilibrium—'fixed point') to regular bursty behaviour (stable periodic non-linear behaviour—'limit cycle'). Reference [7] discusses a simple yet relevant non-linear dynamic model for predicting and interpreting these observations.

The most interesting feature of e$^-$-fishbones is their relevance to burning plasmas. In fact, unlike fast ions in present-day experiments, fast electrons have small orbits, similarly to α particles in reactor-relevant conditions, which do not introduce additional complications in the physics due to non-local behaviours. In this respect, the bounce averaged dynamics of both trapped and barely circulating electrons depends on energy (not mass): thus, their effect on low frequency MHD modes can be used to simulate/analyse the analogous effect of charged fusion products. Moreover, the combined use of ECH and LH provides extremely flexible tools to investigate various nonlinear behaviours, of which FTU experiment provides a nice and clear example (figure 18).

9. Conclusions and perspectives

Considerable amount of work has been carried out in the two years after the previous FEC-2004 within the potentialities of the FTU device in several fields.

The study of the ITBs obtained with electron heating only and no toroidal momentum injection has been extended to regimes where the ion collisional heating is enough to examine its effect on the ITB features. No degradation of the ITB performance has been found, but rather an improvement in the ion transport appears to be consequent to the e$^-$ITB formation: this gives good prospects for ITER, where the main heating will be to electrons and the moment input quite low. Wide steady ITBs ($r_{\rm ITB}/a > 0.65$) are also obtained by acting on the radial absorption of the LH waves, which mainly determines the most suitable current profile. The importance of the LHCD as the main source for ITB formation has been stressed together with its unique possibility of building these regimes during the current plateau phase. This feature is of particular interest since it permits to recover the ITB, should it be lost during a long lasting pulse. Moreover, it makes immaterial the details of the current build-up phase and of the waveforms and the timing of the additional heating, which are instead crucial for building up ITBs with other methods.

Within the wide, important and still open issue of the PFCs, the properties of lithium as PFC have been studied for the first time in a tokamak plasma with density close to ITER. The feasibility of a liquid (Li) as a first wall material has been tested through a LLL of innovative design, based on a capillary porous mesh that faces the main plasma. Despite that only ohmic regimes have been explored so far, the Li liquid limiter has been exposed to thermal load in excess of 5 MW m^{-2}. No damage has been detected on the surface of the limiter, while plasma characteristics have been improved, in terms of lower effective charge, less impurity radiation and much reduced wall particle recycling. Over the entire spanned density range, $0.2 \leqslant \bar{n}_{\rm e} \leqslant 2.7 \times 10^{20}$ m^{-3}, a better control of the plasma density is achieved. New interesting regimes

have been discovered with a strong density peaking and a clear particle transport barrier at the Greenwald density limit, $\bar{n}_e = 2 \times 10^{20}\,m^{-3}$. A crucial role is played by the strong pumping capability of Li.

The flexibility of the ECH system has enabled the development of a real-time fast method to detect and localize the MHD tearing modes. Stabilization of the mode is achieved in a short time and with relatively low power, which is focused just on the island. This same system has been used to investigate the possibility of avoiding/mitigating disruptions. Full disruption prevention is obtained quite promptly if the ECH deposition is much localized onto the surface where the most dangerous MHD activities develop.

As a basic contribution to the ITER diagnostics, the feasibility of the CTS, which is at present the first candidate to diagnose the fast particle distribution, has been investigated. A configuration very similar to ITER, namely, with microwaves at a frequency below the electron resonance, has been used. The main problems of the reliability have been singled out, as being due to the modulation induced on the gyrotron power source by the back reflections.

In the LHCD physics studies, progress have been made in modelling the interaction of the LH waves with the edge plasma, considering either the linear wave scattering by density fluctuations or the non-linear physics involving parametric decay instability, with promising comparisons with the experimental data.

Theoretical activity applied to the FTU experiment has marked important progress in explaining the dynamics of the electron–fishbone instability, developing when at relatively low density the LH generated fast electrons exceed a certain number. These instabilities are responsible for a radial redistribution of the fast particles. The importance of these studies for ITER lies in the fact that the dynamics has many similarities with that of the α particle: the physics that rules the phenomena depends only on energy and not on the mass of the particle, and the fast electrons in FTU have small dimensionless orbits as the α particles in ITER, different from most tokamaks where very wide orbits are associated with fast ions.

The future FTU priorities will be the full testing of the LLL under strong additional heating (LH+ECH) and surface thermal load in excess of $10\,MW\,m^{-2}$. The stability of the liquid surface against disruption will also be assessed, and the new high density/high particle confinement regimes will be characterized in more detail. The study of ITB physics will be mainly focused on the ion transport under greater collisional coupling to electrons. By optimizing the use of the auxiliary heating systems, ITBs with a lower ratio between the thermal e^-–i^+ equipartition time and the energy confinement time, so far always >5, will be accessed. The full automation and a complete feedback loop in the MHD stabilization by local ECCD is also in the future plans, as well as a fast detection of the localization of the killer MHD modes in disruptions. In support of ITER issues, it is planned to investigate deeply the promising capabilities of ECH+LHCD systems in assisting the plasma start-up. The possibility of testing a new transmitting antenna for the CTS, robust against the risk of gyrotron perturbation, is also being considered.

References

[1] Gormezano C. (ed) Special Issue on FTU 2004 *Fus. Sci. Technol.* **45** (May 2004)
[2] Angelini B. *et al* 2005 *Nucl. Fusion* **45** S227–38
[3] Pericoli Ridolfini V. *et al* 2005 *Plasma Phys. Control. Fusion* **47** B285–301
[4] Pericoli Ridolfini V. *et al* 2007 Edge properties with the liquid lithium limiter in FTU—experiment and transport modelling *Plasma Phys. Control. Fusion* submitted
[5] Granucci G. *et al* 2006 Application of ECRH/ECCD on FTU: an overview of recent results *14th Workshop on ECE and ECRH (Santorini, Greece, 9–11 May 2006)*
[6] Tartari U. *et al* 2006 *Nucl. Fusion* **46** 928–40
[7] Zonca F. *et al* 2006 Electron fishbones: theory and experimental evidence *Proc. 21st Int. Conf. on Fusion Energy 2006 (Chengdu)* (Vienna: IAEA) CD-ROM file TH/3-2 and http://www-naweb.iaea.org/napc/physics/FEC/FEC2006/html/index.htm *Nucl. Fusion* submitted
[8] Gormezano C. *et al* 2004 *Plasma Phys. Control. Fusion* **46** B435–47
[9] Moret J.M. *et al* 2004 Progress in the understanding and the performance of ECH and plasma shaping on TCV *Proc. 20th Int. Conf. on Fusion Energy 2004 (Vilamoura)* (Vienna: IAEA) CD-ROM file OV/4-5 and http://www-naweb.iaea.org/napc/physics/fec/fec2004/datasets-index.html
[10] Greenwald M.J. *et al* 2005 *Nucl. Fusion* **45** S109–17
[11] Parker R. 2006 Lower hybrid current drive experiments in Alcator C-Mod *48th Annual Meeting of the Division of Plasma Physics (Philadelphia, PA, USA 30 October–3 November 2006)* DPP06 Meeting Web Bulletin Paper No.: BI1.00001 and http://meetings.aps.org/Meeting/DPP06/Event/51629
[12] Gruber O. *et al* 2001 *Nucl. Fusion* **41** 1369–89
[13] Greenwald M.J. *et al* 1988 *Nucl. Fusion* **28** 2199
[14] Pericoli Ridolfini V. *et al* 2006 Internal transport barriers in FTU at ITER relevant plasma density with pure electron heating and current drive *Proc. 21st Int. Conf. on Fusion Energy 2006 (Chengdu)* (Vienna: IAEA) CD-ROM file EX/P1-15 and http://www-naweb.iaea.org/napc/physics/FEC/FEC2006/html/index.htm
[15] Sozzi C. *et al* 2005 *J. Phys.: Conf. Ser.* **25** 198–209
[16] Pericoli Ridolfini V. *et al* 2003 *Nucl. Fusion* **43** 469–78
[17] Tresset G. *et al* 2002 *Nucl. Fusion* **42** 520–6
[18] Mailloux J. *et al* 2002 *Phys. Plasmas* **9** 2156–64
[19] Castaldo C. *et al* 2002 *Phys. Plasmas* **9** 3205-8
[20] Cesario R. *et al* 2004 *Phys. Rev. Lett.* **92** 175002
[21] Ide S. *et al* 2000 *Nucl. Fusion* **40** 445–51
[22] Kaye S.M. *et al* 1997 *Nucl. Fusion* **37** 1303–28
[23] De Benedetti M. *et al* 2005 Turbulence measurements and improved confinement regimes on FTU *32nd EPS Conf. on Plasma Physics and Controlled Fusion (Tarragona, Spain, 27 June–1 July 2005)* paper P4.035, http://eps2005.ciemat.es/papers/pdf/P4_035.pdf
[24] Pericoli Ridolfini V. *et al* 2007 *Nucl. Fusion* **45** 1386–95
[25] Marocco D. *et al* 2005 Transport analysis of FTU plasmas with multiple pellet injection using neutron-derived Ti profiles and high-resolution ne profiles *Proc. 32nd Conf. on Plasma Physics and Controlled Fusion (Tarragona, Spain 27 June–1 July 2005)* paper P4.033, http://eps2005.ciemat.es/papers/pdf/P4_033.pdf
[26] Castaldo C. *et al* 2006 Modelling of experiments with ITER-relevant q-profile control at high β_N by means of the lower hybrid current drive *Proc. 33rd EPS Conf. on Plasma Phyics (Roma, Italy)* vol 30 I (ECA), http://eps2006.frascati.enea.it/papers/pdf/P1_122.pdf
[27] Cesario R. *et al* 2006 *Nucl. Fusion* **46** 462–76
[28] Cesario R. *et al* 2005 Radio Frequency Power in Plasmas *Proc. 16th Topical Conf. on Radio Frequency Power in Plasmas (Park City, UT, USA, 11–13 April 2005) AIP Conf. Proc.* **787** 295–302

[29] Brooks J.N. *et al* 2005 *Fusion Sci. Technol.* **47** 669–77
[30] Vertkov A. *et al* 2006 Technological aspects of liquid lithium limiter experiment on FTU tokamak *24th Symp. on Fusion Technology (SOFT) (Warsaw, Poland, 11–15 September 2006)* paper N. O3A-F-32
[31] Evtikhin V.A., Lyublinski I.E., *et al* 2001 *Fusion Eng. Des.* **56–57** 363–7
[32] Apicella M.L. *et al* 2007 *J. Nucl. Mater.* **363–365** 1346–51
[33] Alekseyev A. *et al* 2006 Fiber-optic sensor for monitoring of liquid Li limiter surface temperature *Proc. 33rd EPS Conf. on Plasma Physics (Roma, Italy, 19–23 June 2006)* (ECA) vol 30I P1.162, http://eps2006.frascati.enea.it/papers/pdf/P1_162.pdf
[34] Mazzitelli G. *et al* 2006 Lithium as a liquid limiter in FTU *Proc. 21st Int. Conf. on Fusion Energy 2006 (Chengdu)* (Vienna: IAEA) CD-ROM file EX/P4-16 and http://www-naweb.iaea.org/napc/physics/FEC/FEC2006/html/index.htm
[35] Apicella M.L. *et al* 2006 Energy balance of FTU discharges with lithizated walls *Proc. 33rd EPS Conf. on Plasma Physics (Roma, Italy, 19–23 June 2006)* vol 30I (ECA) D5.023, http://eps2006.frascati.enea.it/papers/pdf/D5_023.pdf
[36] Tudisco O. *et al* 2006 Density profile studies of plasmas with lithium limiter *Proc. 33rd EPS Conf. on Plasma Physics (Roma, Italy, 19–23 June 2006)* vol 30I (ECA) P5.072, http://eps2006.frascati.enea.it/papers/pdf/P5_072.pdf
[37] Zagórski R. and Gerhauser H. 2004 *Phys. Scr.* **70** 173
[38] Zagórski R. *et al* 2006 *22nd Symp. on Plasma Pysics and Technology (Praha, Czech Republic, 26-29 June 2006) Czech. J. Phys.* **56** B182–8
[39] Tudisco O. *et al* 2004 *Fusion. Sci. Technol.* **45** Chapter 8 402–21
[40] Esposito B. *et al* 2006 Disruption mitigation experiments in FTU using ECRH *Proc. 33rd EPS Conf. on Plasma Physics (Roma, Italy, 19–23 June 2006)* vol 301 (ECA) P5.071, http://eps2006.frascati.enea.it/papers/pdf/P5_071.pdf
[41] Cirant S. *et al* 2005 *J. Phys.: Conf. Ser.* **25** 223–33
[42] Berrino J. *et al* 2005 *Nucl. Fusion* **45** 1350–61
[43] Lazzaro E. *et al* 2000 *Phys. Rev. Lett.* **84** 6038
[44] Cirant S. *et al* 2000 Mode coupling trigger of tearing modes in ECW heated discharges in FTU *Proc. 18th Int. Conf. in Fusion Energy 2000 (Sorrento)* (Vienna: IAEA) CD-ROM file EX3/3 and http://www.iaea.org/programmes/ripc/physics/fec2000/html/node1.htm
[45] Berrino J. *et al* 2006 Automatic real-time tracking and stabilization of magnetic islands in a tokamak using temperature fluctuations and ecw power *IEEE Transac. Nucl. Sci.* **53** 1009–14
[46] Bindslev H. *et al* 2003 ITER fast ion collective Thomson scattering—feasibility study Annex 1 *Riso Laboratory Report* EFDA Contract 01.654
[47] Prater R. *et al* 1997 *10th Joint Workshop on ECE and ECRH (Ameland, The Netherlands)* (Singapore: World Scientific) pp 531–40
[48] Idei H. *et al* 2006 *Nucl. Fusion* **46** 489
[49] Pericoli-Ridolfini V., Giannone L. and Bartiromo R. 1994 *Nucl. Fusion* **34** 469–81
[50] Pericoli Ridolfini V., Pietropaolo A., Cesario R. and Zonca F 1998 *Nucl. Fusion* **38** 1745–55
[51] Andrews P.L. and Perkins F. 1983 *Phys Fluids* **26** 2537–45
[52] Esterkin A.R. and Piliya A.D. 1996 *Nucl. Fusion* **36** 1501–12
[53] Calabrò G., Pericoli Ridolfini V., Panaccione L. and FTU team Effect of the scattering from edge density fluctuations on the lower hybrid waves in FTU *Proc. 33rd EPS Conf. on Plasma Physics (Roma, Italy, 19–23 June 2006)* vol 30I (ECA) P5–077 http://eps2006.frascati.enea.it/papers/pdf/P5_077.pdf
[54] Wong K.L. *et al* 2000 *Phys. Rev. Lett.* **85** 996
[55] Smeulders P. *et al* 2002 Fast MHD analysis on FTU *Proc. 29th EPS Conf. on Plasma Physics Controlled Fusion (Montreux, Switzerland, 17–21 June 2002)* 26B (ECA) D-5.016, http://epsppd.epfl.ch/Montreux/pdf/D5_016.pdf
[56] Ding X.T. *et al* 2002 *Nucl. Fusion* **42** 491
[57] Sun Y. *et al* 2005 *Plasma Phys. Control. Fusion* **47** 745–56
[58] Chen L. *et al* 1984 *Phys. Rev. Lett.* **52** 1122